ADVANCED MATERIALS INTERFACES
www.advmatinterfaces.de

A Dry-Processed $Al_2O_3/LiAlO_2$ Coating for Stabilizing the Cathode/Electrolyte Interface in High-Ni NCM-Based All-Solid-State Batteries

Rajendra S. Negi, Yuriy Yusim, Ruijun Pan, Shamail Ahmed, Kerstin Volz, Ryo Takata, Franz Schmidt, Anja Henss,* and Matthias T. Elm**

Due to their high theoretical energy densities and superior safety, thiophosphate-based all-solid-state batteries (ASSBs) are considered as promising power source for electric vehicles. However, for large-scale industrial applications, interfacial degradation between high-voltage cathode active materials (CAMs) and solid-state electrolytes (SSEs) needs to be overcome with a simple, cost-effective solution. Surface coatings, which prevent the direct physical contact between CAM and SSE and in turn stabilize the interface, are considered as promising approach to solve this issue. In this work, an $Al_2O_3/LiAlO_2$ coating for $Li(Ni_{0.70}Co_{0.15}Mn_{0.15})O_2$ (NCM) is tested for ASSBs. The coating is obtained from a recently developed dry coating process followed by post-annealing at 600 °C. Structural characterization reveals that the heat treatment results in the formation of a dense $Al_2O_3/LiAlO_2$ coating layer. Electrochemical evaluations confirm that the annealing-induced structural changes are beneficial for ASSB. Cells containing $Al_2O_3/LiAlO_2$-coated NCM show a significant improvement of the rate capability and long-term cycling performance compared to those assembled from Al_2O_3-coated and uncoated cathodes. Moreover, electrochemical impedance spectroscopy analysis shows a decreased cell impedance after cycling indicating a reduced interfacial degradation for the $Al_2O_3/LiAlO_2$-coated electrode. The results highlight a promising low-cost and scalable CAM coating process, enabling large-scale cathode coating for next-generation ASSBs.

1. Introduction

All-solid-state batteries (ASSBs) are one of the most promising approaches to achieve electrical energy storage and transport electrification goals.[1–3] In comparison to state-of-the-art lithium-ion batteries (LIBs) containing liquid electrolyte, ASSBs provide an improved safety due to the non-flammability of the solid-state electrolytes (SSEs) along with the possibility to achieve higher capacity when using a lithium metal anode.[4] So far, several SSEs with high ionic conductivity have been discovered for ASSBs.[4,5] Among them, oxide-based SSEs including garnet ceramics (e.g., $Li_7La_3Zr_2O_{12}$),[6] perovskites (e.g., $Li_{1+x}Al_xTi_{2-x}(PO_4)_3$),[7] and thiophosphate-based SSEs (TSSEs)[8] including $Li_{10}GeP_2S_{12}$ are considered as promising candidates for practical applications.[9] Oxide-based SSEs require high-temperature sintering (>700 °C) to achieve sufficient interfacial contact between SSEs and cathode active materials (CAMs) due to their hard mechanical properties. Unfortunately, the heat treatment causes irreversible

R. S. Negi, R. Pan, A. Henss, M. T. Elm
Center for Materials Research (LaMa)
Justus Liebig University Giessen
Heinrich-Buff-Ring 16, 35392 Giessen, Germany

Y. Yusim, R. Pan, A. Henss, M. T. Elm
Institute of Physical Chemistry
Justus Liebig University Giessen
Heinrich-Buff-Ring 17, 35392 Giessen, Germany
E-mail: Ruijun.Pan@phys.chemie.uni-giessen.de;
Anja.Henss@phys.chemie.uni-giessen.de;
Matthias.Elm@phys.chemie.uni-giessen.de

The ORCID identification number(s) for the author(s) of this article can be found under https://doi.org/10.1002/admi.202101428.

DOI: 10.1002/admi.202101428

R. Pan
Materials Science and Engineering Program and Texas Materials Institute
University of Texas at Austin
Austin, TX 78712, USA

S. Ahmed, K. Volz
Materials Science Centre and Faculty of Physics
Philipps University Marburg
Hans-Meerwein-Strasse 6, 35043 Marburg, Germany

R. Takata, F. Schmidt
Evonik Operations GmbH
Rodenbacher Chaussee 4, 63457 Hanau, Germany

M. T. Elm
Institute of Experimental Physics I
Justus Liebig University Giessen
Heinrich-Buff-Ring 16, 35392 Giessen, Germany

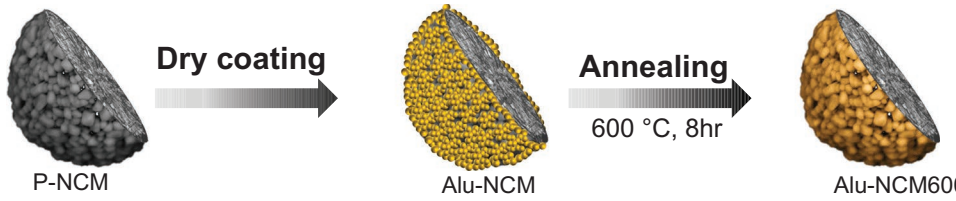

Figure 1. Schematic illustration of the $Al_2O_3/LiAlO_2$ dry coating process and the additional post-annealing process of Ni-rich NCM for ASSBs.

degradation reactions at the electrolyte–electrode interface resulting in increased interfacial resistances.[10–12] In contrast, thiophosphate-based SSEs are rather soft and, thus, provide good interfacial contact to CAMs. Furthermore, they exhibit high ionic conductivities of above 20 mS cm^{-1} at room temperature[3,13] making them more attractive for applications in ASSBs.[14]

Despite numerous advantages of TSSEs, several remaining challenges have to be addressed on the way to large-scale industrial application of ASSBs, such as interfacial stability issues[15,16] between high voltage CAMs and TSSEs. Ni-rich $LiNi_{1-x-y}Co_xMn_yO_2$ (NCM) CAMs are commonly accepted as the state-of-the-art high energy density CAMs for ASSBs with high specific capacities and high working voltages combined with mature industrial-scale production.[17,18] However, inside the cell, NCMs and TSSEs form a cathode–electrolyte interphase (CEI) consisting of degradation products of both.[19] Various studies suggest that the formed CEI layer between CAM and SSE is responsible for long-term capacity fading and limited operational life.[15,20,21] Therefore, research efforts are dedicated to improve the interfacial stability between CAMs and TSSEs.

Surface coating is a well-established strategy to enhance the interfacial stability between CAM and SSE by preventing direct physical contact.[22] For NCM-CAM, oxide-based coatings such as $LiNbO_3$,[23–25] $Li_4Ti_5O_{12}$,[24] Li_2O-ZrO_2,[26] HfO_2,[27] and $Li_3B_{11}O_{18}$[28] have been reported to improve the electrochemical performance of ASSBs, as they effectively prevent or reduce detrimental side reactions at the NCM/SSE interface. In conventional LIBs, Al_2O_3-based coatings have been considered as promising coatings due to their effectiveness against side reactions and low synthesis cost.[29–32] However, they are not well explored in ASSBs yet.[33–36] Although Al_2O_3-based coatings enhance the interfacial stability, the rate capability could not be improved significantly, primarily due to the ionically and electronically insulating nature of the coating.[37] In contrast, $LiAlO_2$ provides good lithium-ion transport properties due to partially occupied Li sites.[38] This means that $LiAlO_2$ or mixed $Al_2O_3/LiAlO_2$ coating layers stabilize the CAM/SSE interface effectively without significantly increasing the interfacial resistance.[39,40] Thus, $LiAlO_2$-based coatings could be promising candidates to improve the overall performance of ASSBs.

Surface coatings on cathode materials using wet-chemical approaches,[41] atomic layer deposition (ALD),[42] or spray coating procedures[24,43] are already successfully established in thiophosphate-based ASSBs.[44] However, wet-chemical approaches require additional drying steps that increase the energy costs and manufacturing time.[45] While the ALD technology provides thin coating layers with excellent conformity, it often requires toxic precursors and shows slow deposition rates.[34,46,47] With spray coating procedures, the manufacturing time can be reduced, but an expensive piece of instrument is needed.[44]

In order to reduce ecological and economic costs, a new dry coating procedure on CAM was recently introduced by Herzog et al.[34] It has been shown that by using a high energy mixer, fumed nanostructured Al_2O_3 physically absorb on the surface of NCM particles and form a porous Al_2O_3-coating layer, which significantly improves the electrochemical rate performance and capacity retention in liquid-electrolyte-based LIBs.[34]

In the study presented here, we modified the dry coating procedure by using an additional annealing step in order to make it more suitable for thiophosphate-based ASSBs and to achieve a dry-processed $Al_2O_3/LiAlO_2$ coating for $Li(Ni_{0.70}Co_{0.15}Mn_{0.15})O_2$ (NCM701515) CAM. The high-temperature treatment is found to improve various aspects of the coating (such as better interface formation, reduced porosity, and thickness), which altogether significantly improve the electrochemical performance of the NCM-based ASSBs in terms of the C-rate and long-term cycling performance. The full cells with coated NCM cathodes show a decreased interfacial impedance, which indicates a better interfacial stability between CAM and TSSE. Our results highlight that the low-cost and simple dry coating process without any detrimental environmental solvents is a highly promising approach for large-scale industrial production of coated cathode active material for next-generation ASSBs.

2. Results and Discussion

2.1. Characterization of the Al_2O_3- and $Al_2O_3/LiAlO_2$-Coated NCM

Figure 1 shows a schematic illustration of the dry coating process used to coat NCM secondary particles with $Al_2O_3/LiAlO_2$. As described in the Experimental Section, the Al_2O_3 powder was mixed with the NCM powder in a high-energy mixer to achieve an Al_2O_3 coating on the surface of the NCM secondary particles (denoted as Alu-NCM) in the first step. In a second step, the Alu-NCM was divided into two batches. One of the batches was annealed at 600 °C for 8 h, resulting in the conversion of Al_2O_3 to $Al_2O_3/LiAlO_2$ (denoted as Alu-NCM600). The formation of $Al_2O_3/LiAlO_2$ is confirmed by X-ray photoelectron spectroscopy (XPS) as will be discussed later. The principle of the dry coating process is described in detail by Herzog et al.[34] In brief, during high energy mixing, nanostructured fumed Al_2O_3 powder produced from flame hydrolysis is deagglomerated into smaller aggregates with a high specific surface area. This ensures a good adhesion capability of the aggregates at the CAM surface, which

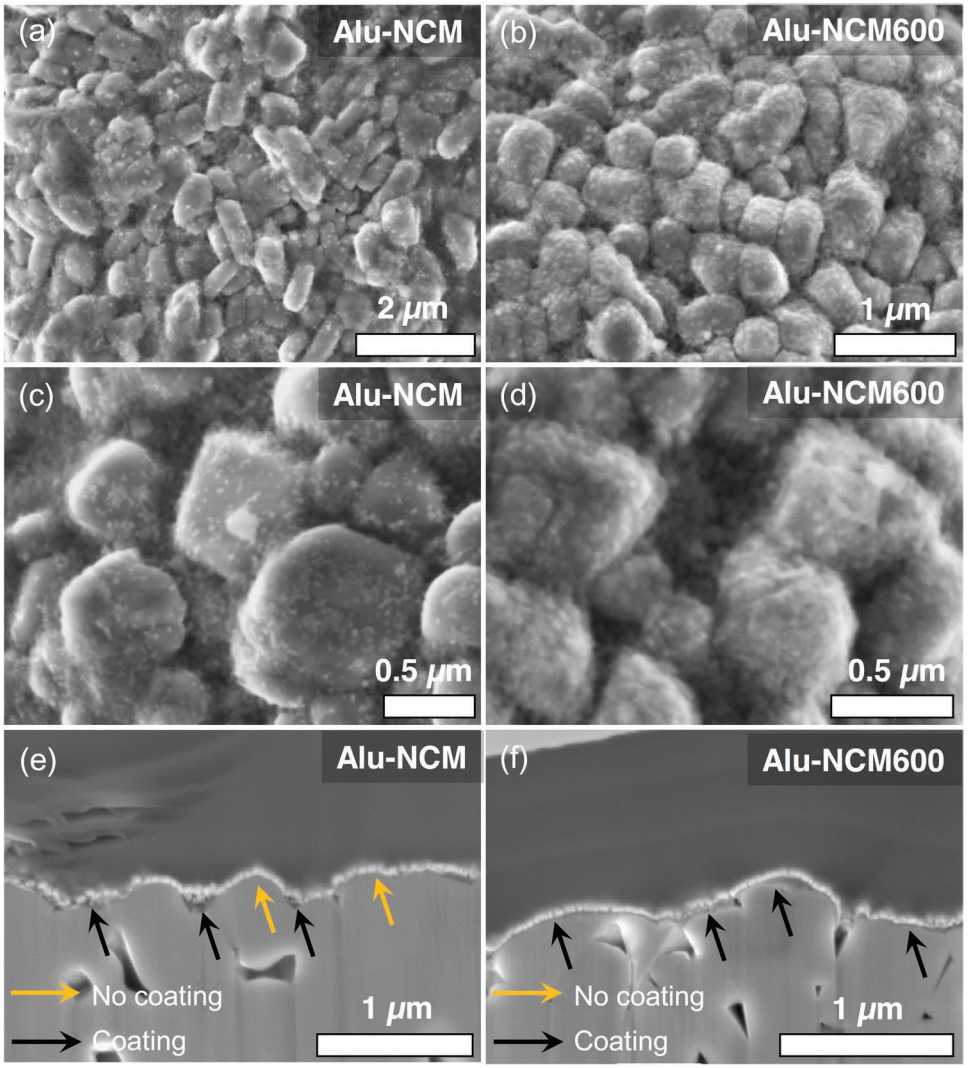

Figure 2. SEM images of the coated NCM powder: a,c) Alu-NCM and b,d) Alu-NCM600. SEM cross-section images of coated NCM secondary particles: e) Alu-NCM and f) Alu-NCM600. For Alu-NCM the coating is only observable between the NCM grains as particles (black arrow), f) while for Alu-NCM600 a homogeneous coating is detectable as a dark line between NCM and the deposited Pt layer (white layer).

is decisive for the formation of a complete and strongly adherent coating layer.[34] Due to the short processing time, easy application, and solvent-free nature, the dry coating process is a promising method for large-scale production at low costs.

The NCM-based CAM with an Al_2O_3 and $Al_2O_3/LiAlO_2$ coating layer was investigated by scanning electron microscopy (SEM). As shown in Figure S1 in the Supporting Information, the secondary particles of the uncoated NCM are spherical in shape with a diameter of 5–15 µm and are composed of nano-sized primary particles. The SEM images in **Figure 2**a–d show a comparison between Alu-NCM and Alu-NCM600. It can be seen that in both cases, the coated NCM reveals a narrow size distribution of the primary particles, which agrees well with those of the uncoated NCM primary particles (see Figure S1, Supporting Information). This indicates that the mixing intensity is strong enough to break the fumed Al_2O_3 agglomerates and to coat the secondary NCM particles while maintaining their structural integrity during the dry coating process.

However, the surface of non-annealed Alu-NCM shows significant differences compared to that of Alu-NCM600. After the coating process, the Al_2O_3 looks inhomogeneously distributed with incomplete coverage of the NCM surface. In contrast, the coating seems to be fused after the annealing step, resulting in a very homogeneous and complete coverage of the NCM surface. Focused-ion beam (FIB)-SEM analysis was carried out to compare the cross-section of the NCM particles after coating and annealing. In Figure 2e, the coating without annealing looks rough and is mainly accumulated in the gaps between neighboring primary NCM particles. However, as shown in Figure 2f, the coating after annealing is much smoother and completely distributed over the surface with slight variations of the thickness (see also Figure S2, Supporting Information). In addition, SEM images of Alu-NCM and Alu-NCM600 with higher magnification are shown in Figure S3a,b in the Supporting Information. SEM-energy dispersive spectroscopy (EDS) mapping confirms the homogeneous distribution of Al

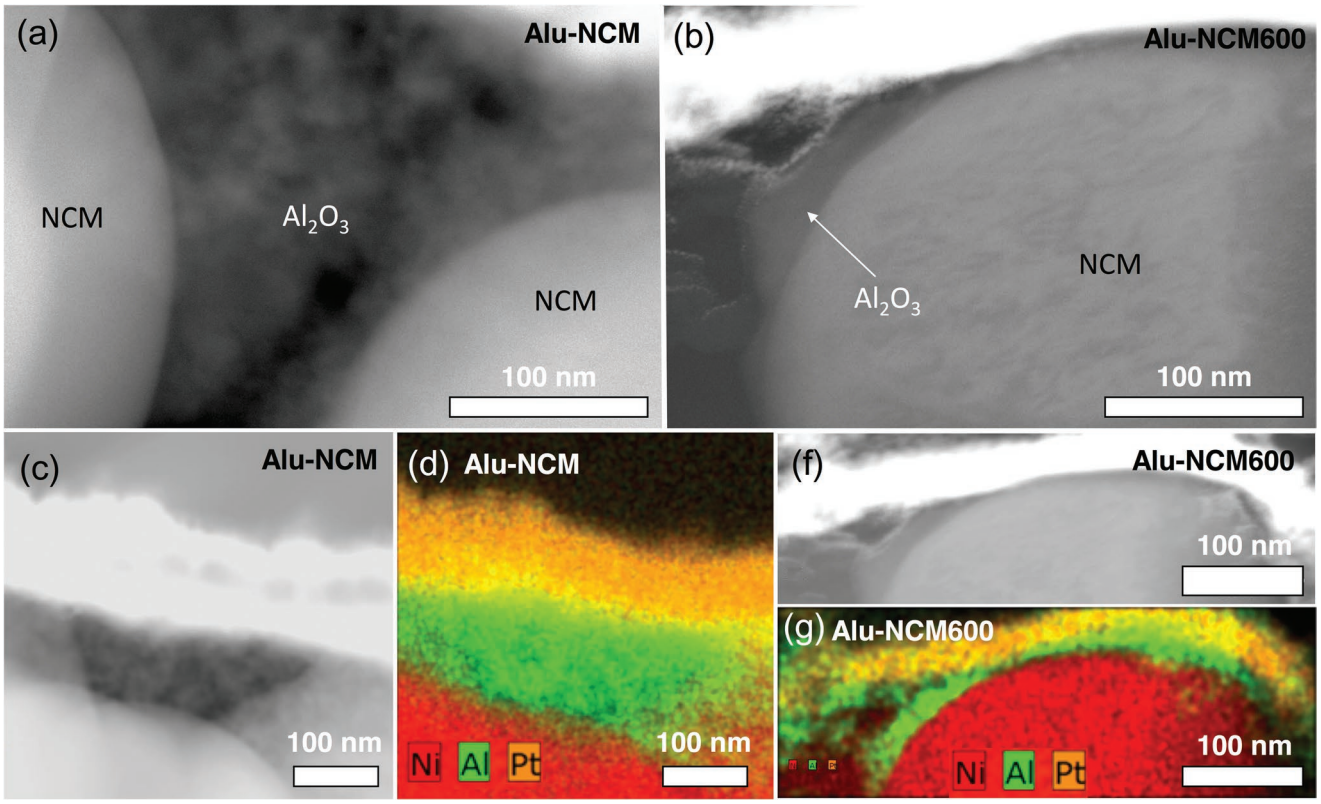

Figure 3. STEM-HAADF images of a cross-section of coated NCM701515: a,c) Alu-NCM and b,f) Alu-NCM600. STEM-EDS analysis of a cross-section of coated NCM701515 showing a three-color superposition image of Ni, Al, and Pt: d) Alu-NCM and g) Alu-NCM600.

on Alu-NCM600 as shown in Figure S3c in the Supporting Information.

For a more detailed surface analysis, the microstructure of the coating layer was characterized by transmission electron microscopy (TEM) in combination with EDS.[48] As shown in **Figure 3**a,c, for Alu-NCM, the coating layer is highly porous as observed by Herzog et al.[34] Figure 3a shows that the gaps between the primary NCM particles are completely filled with Al_2O_3, leaving the surface uncovered. On the other hand, in the case of Alu-NCM600 (Figure 3b,f), the coating layer is less porous and much thinner after the annealing step. No structural changes of the NCM particles are observable. Only the structural properties of the coating are affected by the additional annealing step. EDS analysis confirms the drastic change of the coating thickness and porosity after annealing (Figure 3d,g). There are no hints for the diffusion of aluminum into the NCM bulk phase observable for the non-annealed Alu-NCM sample. This is expected as no high-temperature step is involved in the coating process and aluminum diffusion is unlikely to occur at room temperature.[34] However, in case of Alu-NCM600 (Figure 3g) the possibility of interdiffusion of a small Al amount into the NCM bulk structure during annealing cannot be excluded.[49] As reported in literature, the interdiffusion of Al between the CAM and the coating layer may enhance the overall stability of the CAM and lead to improved cycling performance.[50] However, a detailed discussion of aluminum diffusion into the NCM bulk is beyond the scope of this study.

The porosity of the CAM particles after the coating process was investigated by N_2 adsorption. The measurements were evaluated using the Brunauer–Emmett–Teller (BET) model. As shown in **Figure 4**a, the uncoated NCM has a very low BET surface of 0.40 $m^2\ g^{-1}$. After coating with fumed Al_2O_3, the BET surface area increases drastically to 0.70 $m^2\ g^{-1}$ (Alu-NCM sample), which is well expected due to the high porosity of the coating as observed by TEM measurements (Figure 3c). After the annealing step (Alu-NCM600 sample), the BET area is significantly decreased (0.50 $m^2\ g^{-1}$). This confirms that the annealing step leads to a densification of the coating layer and a lower surface area.

Powder X-ray diffraction (XRD) measurements were carried out on P-NCM, Alu-NCM and Alu-NCM600 samples to investigate the potential influence of the coating process on the crystal structure of NCM. As shown in Figure 4b, the XRD patterns confirm that all NCM samples exhibit the same crystal structure of $LiCoO_2$ (space group *R-3m*). No peak shifts are observed, confirming that no significant bulk crystallographic defects are generated in the NCM structure during coating or the annealing step. In addition, both coated samples show no additional peaks belonging to Al_2O_3 due to the low amount of coating material, as observed in our previous study.[39]

XPS measurements were carried out to investigate the coating composition and the effect of annealing on the structural properties of the coating layer. The NCM XPS analysis delivers quantitative element and compound-specific information with a detection limit of about 1 at%.[51] The survey

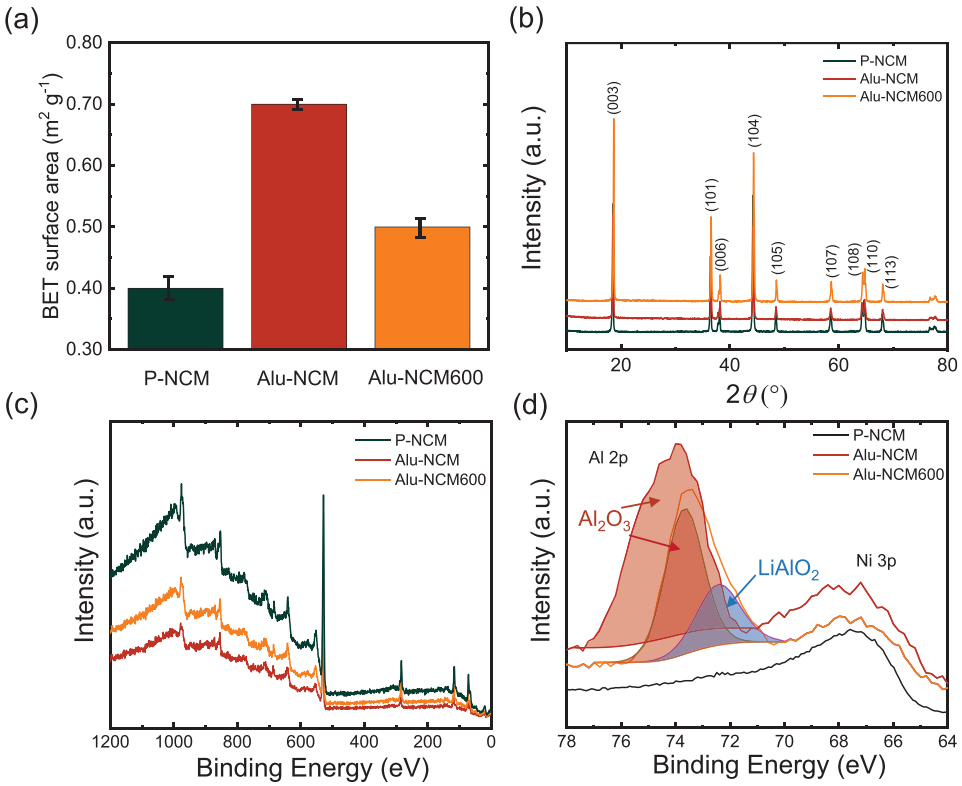

Figure 4. Comparison of a) Brunauer–Emmett–Teller (BET) measurements, b) X-ray diffraction pattern, c) survey XP spectra, and d) detailed XP spectra of P-NCM, Alu-NCM, and Alu-NCM600.

spectrum of P-NCM shown in Figure 4c confirms the presence of Ni, Co, Mn, and O without any additional elements apart from the carbon contaminations at the NCM surface, which is commonly used as a calibration reference for X-ray photoelectron (XP) spectra.[52] In addition, the characteristic peak of Al 2p is detected on the surface of Alu-NCM and Alu-NCM600, which proves the existence of Al species on the surface of the coated NCM with Al_2O_3 (Figure 4d). A detailed spectrum in the region between 78 and 64 eV is shown in Figure 4d. It includes the Al 2p core levels and the Ni 3p peak. No peak shift is observed for the Ni 3p peak for all samples, which additionally confirms the structural stability of NCM during the coating and annealing processes. However, the presence of Ni implies that the coating is not completely covering the NCM surface or, alternatively, thinner than the typical probing depth of XPS of about 3–7 nm,[53] as already indicated by the TEM measurements shown in Figure 3f,g. Deconvolution of the Al 2p peak (Figure 4d) reveals that Alu-NCM shows only one peak at a binding energy of 73.9 eV, which is distinctive for Al atoms in an oxygen environment, such as Al_2O_3 or $Al(OH)_3$.[35] However, after annealing a significant peak shift of Al 2p to a lower binding energy is observed. The deconvolution confirms that the signal comprises two different peaks. One at a binding energy of 73.9 eV (corresponding to Al_2O_3 or $Al(OH)_3$)[53] and a second one at 72.8 eV, which is attributed to $LiAlO_2$ as observed by Tang et al.[54] The results confirm the conversion of an insulating Al_2O_3 coating into an ion conducting $Al_2O_3/LiAlO_2$ coating during heat treatment, as discussed in detail in previous studies.[39,40] The diffusion of Li^+ from NCM into the Al_2O_3 layer during the heat treatment is expected to result in the formation of conductive pathways for the Li^+ ions and thus an improvement of the ionic conductivity of the $Al_2O_3/LiAlO_2$ coating.[39]

The results reveal the tremendous effect of the annealing step on the structural properties of the coating layer, which are illustrated in **Figure 5**. The recently developed dry coating process enables the successful deposition of an Al_2O_3 coating on the surface of NCM particles. The coating is rather thick, porous, and inhomogeneously distributed on the surface of NCM. After annealing at 600 °C, various aspects of the coating morphology are improved. The coating becomes more homogenous (SEM, FIB-SEM), thinner (SEM, TEM), and exhibits a lower porosity, i.e., lower surface area as confirmed by TEM and BET. In addition, the diffusion of Li^+ into the coating results in the conversion from an insulating Al_2O_3 coating layer to $Al_2O_3/LiAlO_2$, which is known to exhibit an improved Li^+ conductivity. All these changes are expected to affect the electrochemical performance of NCM, as will be discussed in detail in the next section.

2.2. Electrochemical Characterization

To elucidate the impact of the obtained microstructural and compositional differences of the two different coatings on the cell performance, we assembled and cycled ASSB cells at different C-rates. The C-rate was varied between 0.1 and 2 C,

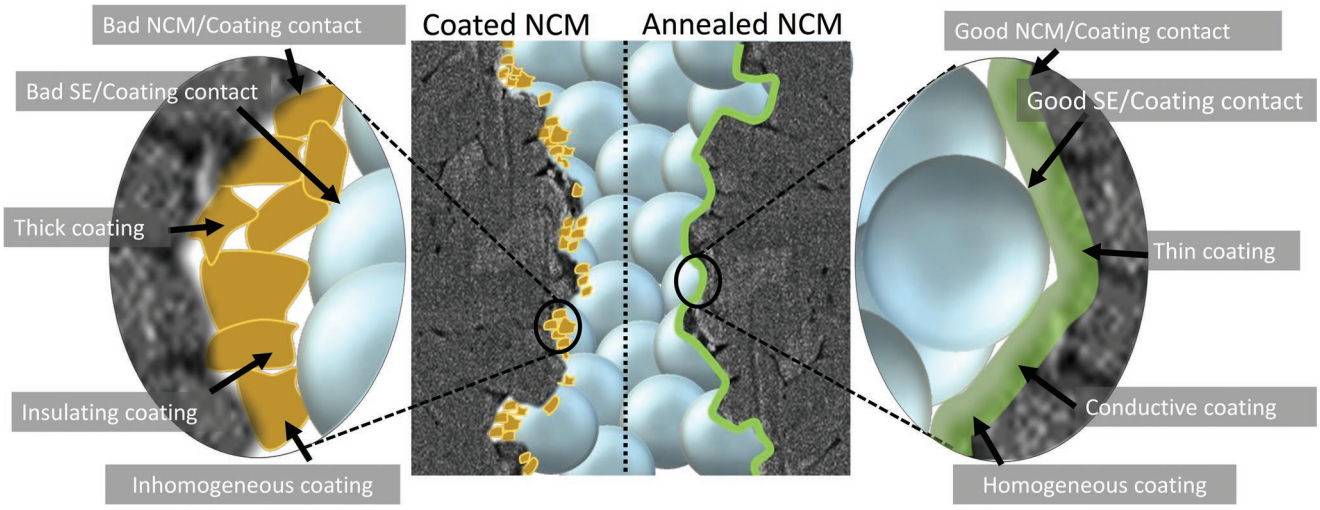

Figure 5. Schematic illustration comparing the differences in coating properties before and after annealing.

within the voltage window of 2.0–3.7 V (vs In/InLi), exceeding the electrochemical stability window of thiophosphate-based SSEs (1.7–2.3 V vs Li^+/Li).[55] The rate capability tests and the long-term cycling stability were investigated for two independent cells in all three cases to ensure reproducibility of the results.

Figure 6a shows the rate capability performance of the coated CAMs in comparison with the performance of the uncoated ones. For a better comparison, Figure 6b also shows the normalized discharge capacity, i.e., the specific discharge capacity of each cell was normalized to the CAM mass and related to the initial specific discharge capacity. The initial specific discharge capacity of the P-NCM cells (136 mAh g^{-1}) is found significantly lower compared to cells with liquid electrolytes (≈ 180 mAh g^{-1})[34,39] indicating a higher interfacial degradation of the SSE than for cells with liquid electrolytes (as the achievable theoretical capacity of NCM is ≈ 180 mAh g^{-1}) as reviewed by Jena et al.[56] The Alu-coated NCM material shows a slightly lower initial specific capacity (130 mAh g^{-1}) than the P-CAM. This indicates that the insulating nature of the Al_2O_3 coating along with its structural properties (such as porosity, insufficient contact area, and interfacial degradation) limits the initial discharge capacity. In contrast, Alu-NCM600 shows a significantly higher initial specific discharge capacity (154 mAh g^{-1}). This is attributed to a lower interfacial resistance, either due to the higher Li^+ conductivity of the Al_2O_3/$LiAlO_2$ coating layer, an increased contact area, or improved interfacial stability (as discussed in the previous section). Furthermore, with increasing C-rate, the discharge capacity of Alu-NCM tends to be slightly superior to P-NCM, revealing the protective effect of the Al_2O_3 coating. However, at a C-rate of 2 C, both the P-NCM and the Alu-NCM samples exhibit no capacity, probably caused by a high internal cell resistance. However, a significant improvement of the C-rate performance in our ASSBs is observed for the Alu-NCM600 samples for all C-rates. In particular, Alu-NCM600 shows a discharge capacity of ≈20 mAh g^{-1} even at 2 C. These results indicate that at high C-rates, a sufficient lithium-ion conductivity still persists in the Al_2O_3/$LiAlO_2$ coating layer, while in the case of the uncoated NCM, the formation of an insulating CEI caused by electrolyte degradation impedes lithium-ion exchange between electrode and electrolyte. Thus, the less porous and more conductive Al_2O_3/$LiAlO_2$ coating material in Alu-NCM600 enables a superior rate capability as compared to Al_2O_3-coated Alu-NCM samples. It is worth noting that the Al_2O_3-dry coating is very effective in improving the electrochemical performance of liquid electrolyte-based cells, as recently shown by Herzog et al.[34] One main reason is that the liquid electrolyte can penetrate into the highly porous Al_2O_3 coating, which facilitates the transport of lithium ions through the surface layer. In contrast, the solid electrolyte used in ASSBs is not able to reach the interior of the pores of the coating (Alu-NCM), i.e., the porous coating impedes lithium-ion transport between active material and electrolyte due to its insulating properties and the reduced contact area. Thus, the results highlight that effective coatings for ASSBs need to fulfill other demands regarding their structural properties than coatings used for liquid-electrolyte-based LIBs.

After the C-rate capability tests, the long-term cycling performance was investigated. Figure 6c compares the discharge capacity and the coulombic efficiency (CE) of pristine NCM, Alu-NCM, and Alu-NCM600 for 100 cycles at 0.25 C in the voltage range between 2.0 and 3.7 V (vs In/InLi). A significantly improved capacity retention is found for Alu-NCM600, which exhibits a discharge capacity of 75 mAh g^{-1} after 100 cycles implying capacity retention of 54% based on the first cycle capacity. In contrast, for the P-NCM sample, a capacity of only 25 mAh g^{-1}, i.e., capacity retention of 20%, is achieved. Furthermore, the corresponding CE of the Alu-NCM600 is superior compared to that of the uncoated sample. As shown in Figure 6d,e, the increase in overpotential is much higher for P-NCM than for Alu-NCM, indicating a more severe electrolyte degradation at the P-NCM surface. The Alu-NCM sample shows a similar behavior as P-NCM during long-term cycling. Although the Al_2O_3 coating certainly suppresses the electrolyte degradation at the NCM-electrolyte interface, its insulating nature, along with the rather worse coating properties, is responsible for a high interfacial resistance, which explains the poor cycling performance. However, the results confirm that

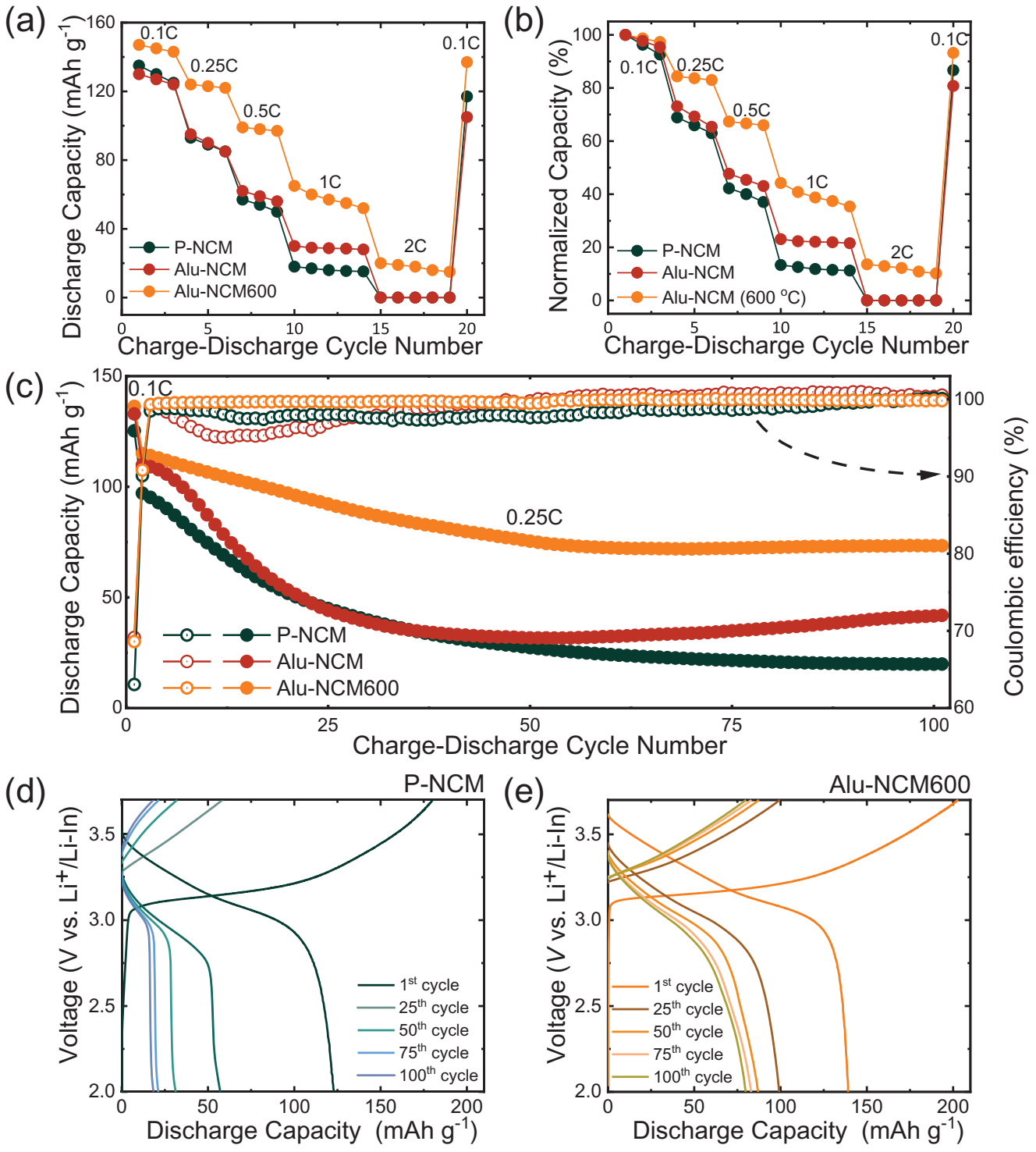

Figure 6. Comparison of a) rate capability and b) corresponding normalized capacity plot of P-NCM, Alu-NCM, and Alu-NCM600. c) Long-term cycling capability at 0.25 C of P-NCM, Alu-NCM, and Alu-NCM600. d,e) Charge–discharge voltage profiles of P-NCM and Alu-NCM600, respectively. The cells were cycled in a voltage window of 2.0 and 3.7 V versus In|InLi, corresponding to 2.6–4.3 V versus Li^+/Li at 25 °C.

the Al_2O_3/$LiAlO_2$ coating significantly improves the long-term cycling stability of NCM in ASSBs. The coating is expected to prevent side reactions between Li_6PS_5Cl (LPS) and NCM, which lead to the formation of a highly resistive CEI consisting of sulfur and phosphorus pentasulfide oxidation products.[19]

To support this assumption, electrochemical impedance spectroscopy (EIS) measurements were carried out on ASSB cells containing P-NCM or Alu-NCM600 as EIS allows to distinguish between different processes in ASSBs and to determine their contribution to the total impedance of the cells.[15,16,57]

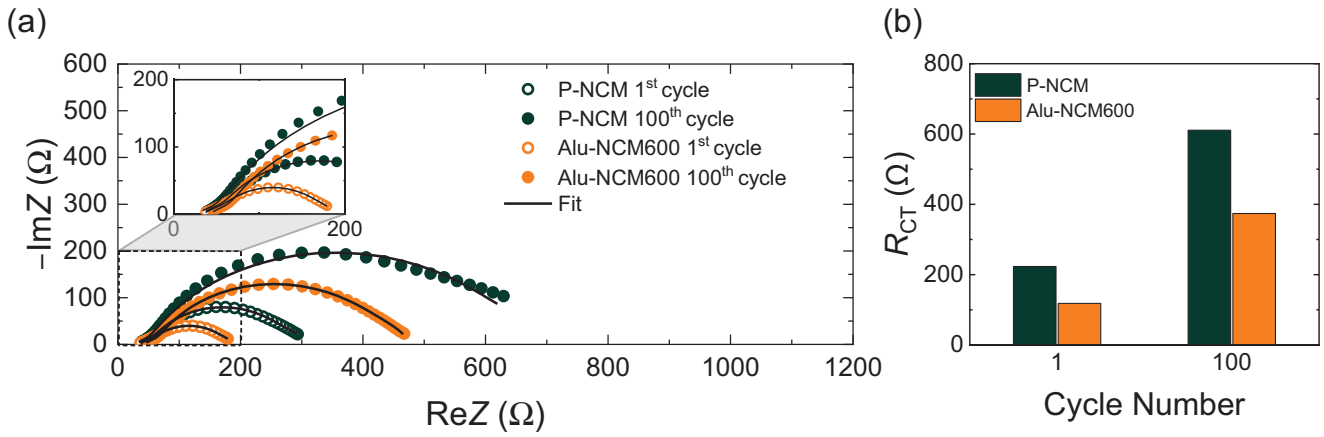

Figure 7. Comparison of a) Nyquist plots of the impedance of full cells containing P-NCM and Alu-NCM600 after the 1st and 100th cycle. b) Corresponding charge transfer resistance R_{CT} measured at an open-circuit voltage of 3.1 V.

As no drastic improvement of the cycling capability is found for the Alu-NCM samples, only P-NCM and Alu-NCM600 are investigated. The EIS measurements were performed at an open-circuit potential of 3.1 V (vs In/InLi) after the 1st cycle and 100th cycle to determine the long-term impedance evolution. A constant potential step was included after constant-current discharge in order to achieve an equilibration of Li within the CAM particles by diffusion processes. This step is necessary to ensure comparability between P-NCM and Alu-NCM600 as the impedance of layered oxide cathode materials depends on the lithium content (state of charge) of the electrode.[58] Comparing the impedance spectra after the 1st and 100th cycle, displayed in **Figure 7**a, a distinct increase of the impedance is observed for the pristine sample indicating a strong degradation reaction at the SSE/CAM interface due to the oxidation of the solid electrolyte.[16,21] The total impedance of the coated NCM cell is significantly lower after the 1st and 100th cycle, corroborating the protection function of the $Al_2O_3/LiAlO_2$ coating. The spectra were fitted using the transmission line model, which describes the impedance of porous electrodes considering SSE-filled pores.[59,60] Due to the presence of nonblocking conditions and negligible electronic conductivity, a Bisquert Open element[61] was used to fit the composite cathode (CC) impedance. The equivalent circuit model, including the Bisquert open element, is described in more detail in Figure S4 in the Supporting Information. The fitting reveals that the differences in the impedance are mainly caused by changes in the charge transfer resistance R_{CT}. The other fitting parameters, such as the anode contribution or the ionic resistance of the electrolyte, do not differ significantly for the different cells (see Table S1, Supporting Information). The determined values of the charge transfer resistance R_{CT} after the 1st and 100th cycles for the pristine and coated samples are shown in Figure 7b. As is evident, the charge transfer resistance of the Alu-NCM600-containing cell is significantly lower not only after the 1st but also after the 100th cycle. Moreover, the comparison with the other impedance values obtained from the fitting (Table S1, Supporting Information) demonstrates that the impedance of the full cell is dominated by the charge transfer resistance of the composite cathode. The comparison of the R_{CT} values confirms that the $Al_2O_3/LiAlO_2$ coating layer significantly improves the interfacial stability by reducing oxidative interfacial decomposition of the SSE on the cathode side.

3. Conclusions

In this study, we present a low-cost, straightforward, and scalable dry coating process to modify the surface of Ni-rich NCM for thiophosphate-based ASSBs. A highly efficient $Al_2O_3/LiAlO_2$ coating is achieved by a high-energy mixing process followed by a high-temperature annealing step. While the Al_2O_3 coating shows a certain porosity after the coating process, the annealing step results in the formation of a dense and thin coating layer as confirmed by TEM and BET measurements. Furthermore, XPS analysis confirms that a mixed $Al_2O_3/LiAlO_2$ layer is formed during the heat treatment, while no significant changes in bulk NCM are observed. Electrochemical characterization demonstrates that the $Al_2O_3/LiAlO_2$ coating significantly improves the electrochemical performance of NCM cathodes in LPS-based ASSBs. As the coating prevents the direct contact between CAM and thiophosphate-based SSE, interfacial degradation reactions responsible for the formation of an insulating CEI are reduced, as demonstrated by EIS analysis. Compared to the porous Al_2O_3 coating, the $Al_2O_3/LiAlO_2$ coating layer provides an improved rate capability and long-term cycling performance, including higher initial cycling capacity. Thus, the results present a highly effective dry coating method, which is suitable for large-scale processing of cathodes for next-generation ASSBs, excluding any solvent-related influences and costs.

4. Experimental Section

Surface Modification of Ni-Rich NCM Using an Al_2O_3-Dry Coating Process: Commercial $Li(Ni_{0.70}Co_{0.15}Mn_{0.15})O_2$ (NCM701515, Linyi Gelon LIB. Co.) was used as CAM and nanostructured fumed Al_2O_3 (AEROXIDE Alu 65, primary particle ≈12 nm, Evonik Operations GmbH) powder was utilized as coating material during the dry-coating process. A lab-scale high-energy Somakon mixer MP-GL (Somakon Verfahrenstechnik UG) was used for mixing. Two different steps were performed for the dry-coating process. Initially, the CAM powder was well mixed with nanostructured Al_2O_3 (1 wt%) at 500 rpm for 1 min.

Subsequently, the mixing intensity was raised to 2000 rpm for 6 min to achieve a well-distributed coating on the surface of the CAM. Then, the powder obtained was divided into two batches. The first batch was dried and transferred into the glovebox for further use (denoted as Alu-NCM). The second batch was additionally annealed at 600 °C for 8 h to modify the coating layer. Subsequently, it was dried and transferred to the glovebox for further use (denoted as Alu-NCM600).

During the first step of the dry-coating process, the fumed nanostructured Al_2O_3 deagglomerates into smaller aggregates and interacts with the cathode surface, resulting in smaller Al_2O_3 aggregates with very strong adhesion to the CAM surface. During the second step, at higher mixing rotation, desirable densification and coalescence of Al_2O_3 aggregates is achieved on the surface of the cathode, which results in a highly homogenous coating.

Materials Characterization: The surface morphology and the elemental composition of the pristine and coated NCM were investigated with SEM (Merlin, Zeiss) at an accelerating voltage of 7 kV and a current of 3000 pA. FIB cross-sections of the coated secondary particles were prepared by a dual-beam JEOL JIB-4601 FIB -SEM. First, a thin layer of platinum was deposited on the surfaces of the coated secondary particles via a Leica EM ACE600 sputter coater before loading them to the FIB-SEM. This is done to protect the coated surfaces of the secondary particles coming in direct contact with the electron beam during FIB cross-section preparation. On top of the thin platinum coating, thick carbon and tungsten protective layers were deposited, respectively, using a Ga-ion beam to further protect the surfaces from Ga-ion beam damage during FIB milling. The samples were milled down using a 30 kV Ga-ion beam to roughly about 200 nm and further thinned down using a 5 kV Ga-ion beam to electron transparency. A double Cs-corrected JEOL 2200-FS microscope was used for scanning TEM (STEM) high-angle annular dark-field (HAADF) imaging and EDS. The microscope was operated at 200 kV.

Powder XRD diffractograms of pristine and coated NCM were obtained using an Empyrean XRD (Panalytical) system with Cu Kα radiation. The XPS analysis was performed using a PHI5000 Versa Probe II (Physical Electronics GmbH) with an Al anode. The pass energy of the analyzer was fixed at 93.5 eV and 23.5 eV to obtain the survey and the detailed spectra, respectively. The chamber pressure was maintained below 10^{-7} Pa. Furthermore, Brunauer–Emmett–Teller (BET) analysis was performed on pristine and coated NCM in order to determine the porosity change after coating and heat treatment. Single point BET was performed using a MICROMERITICS TRISTAR 3000 with a nitrogen/helium flow (28.6% N_2). The samples were degassed for 20 min at 150 °C before the measurement.

Composite Cathode: The CC comprise the pristine or coated $Li(Ni_{0.70}Co_{0.15}Mn_{0.15})O_2$ (NCM701515), LPS (NEI Corporation), and vapor-grown carbon fibers (VGCFs, Sigma-Aldrich Inc., iron-free). At first, NCM and LPS powders were mixed in a mass ratio of 70:30 (volume ratio 47:53). Then, 3 wt% of VGCF was additionally added (exact mass ratio 68:29.1:2.9 (NCM: LPS:VGCF)) to the mixture. Finally, the resulting mixture was hand grounded using an agate mortar for 15 min.

Cell Assembly: The composite cathode was prepared fresh before preparing the cells in order to avoid time-dependent side reactions. All the electrochemical tests were performed using an in-house (pellet type) cell casing.[15,16] For cell assembly, one side of the poly(ether-ether-ketone) (PEEK) cylinder (inner diameter: 10 mm) was closed using a stainless-steel stamp. 60 mg of LPS was uniformly put into the PEEK cylinder, followed by a manual hand compression. Subsequently, 12 mg of CC was added to one side of the pressed LPS and distributed uniformly. The whole stack was then pressed uniaxially at 30 kN (380 MPa) for a duration of 3 min, resulting in a pressed pellet with a thickness of 430 µm (400 µm SSE and 30 µm SSE). An indium foil (In, chemPUR GmbH, diameter = 9 mm, thickness = 125 µm) and a lithium foil (Li, Albermarle (Rockwood Lithium GmbH), diameter = 9 mm, thickness = 120 µm) were placed on the other side of the pellet as an anode. Then, the whole stack was closed using another stainless-steel stamp. Finally, the complete cell assembly was fully closed. During electrochemical characterization, an external frame under constant pressure of ≈50 MPa was used around the cell casing.

Electrochemical Characterization: For electrochemical characterization, Maccor inc. potentiostats/galvanostats and VMP-300 potentiostats (Biologic) were used. The cycling tests (i.e., C-rate and long-term cycling tests) were performed on Maccor inc., while the electrochemical impedance spectroscopy (EIS) measurements were performed on VMP-300. The cells were cycled in a voltage window of 2.0 and 3.7 V versus In|InLi, corresponding to 2.6–4.3 V versus Li^+/Li at 25 °C. For the C-rate tests, the cells were cycled up to 2 C, 1 C = 200 mA g^{-1} (three cycles at 0.1 C, three cycles at 0.25 C, three cycles at 0.5 C, five cycles at 1 C) and five cycles at 2 C). For the long-term cycling, the cells were cycled at 0.1 C for one cycle, followed by 100 cycles at 0.25 C. EIS measurements were performed after the 1st and 100th cycle. All EIS measurements were performed in the frequency range between 7 MHz and 50 mHz, applying a 10 mV AC bias. To ensure reproducibility, every electrochemical experiment was performed with two independent cells.

Supporting Information

Supporting Information is available from the Wiley Online Library or from the author.

Acknowledgements

R.S.N. and Y.Y. contributed equally to this work. R.S.N. and M.T.E. thank the German Federal Ministry of Education and Research (BMBF) for the funding of the NanoMatFutur project NiKo (03XP0093). S.A. and K.V. acknowledge the Federal Ministry of Education and Research (BMBF, Germany) within the cluster of competence FESTBATT (project 03XP0176D).

Open access funding enabled and organized by Projekt DEAL.

Conflict of Interest

The authors declare no conflict of interest.

Data Availability Statement

The data that support the findings of this study are available from the corresponding author upon reasonable request.

Keywords

all-solid-state batteries, electrolyte–electrode interface modification, lithium-ion batteries, solid-state electrolytes, surface coatings on cathode materials

Received: August 5, 2021
Revised: August 20, 2021
Published online: November 9, 2021

[1] G. E. Blomgren, *J. Electrochem. Soc.* **2017**, *164*, A5019.
[2] D. Liu, W. Zhu, Z. Feng, A. Guerfi, A. Vijh, K. Zaghib, *Mater. Sci. Eng. B* **2016**, *213*, 169.
[3] Y. Kato, S. Hori, T. Saito, K. Suzuki, M. Hirayama, A. Mitsui, M. Yonemura, H. Iba, R. Kanno, *Nat. Energy* **2016**, *1*, 16030.
[4] J. Janek, W. G. Zeier, *Nat. Energy* **2016**, *1*, 16141.
[5] J. M. Tarascon, M. Armand, *Nature* **2001**, *414*, 359.

[6] S. Ramakumar, C. Deviannapoorani, L. Dhivya, L. S. Shankar, R. Murugan, *Prog. Mater. Sci.* **2017**, *88*, 325.
[7] M. Monchak, T. Hupfer, A. Senyshyn, H. Boysen, D. Chernyshov, T. Hansen, K. G. Schell, E. C. Bucharsky, M. J. Hoffmann, H. Ehrenberg, *Inorg. Chem.* **2016**, *55*, 2941.
[8] N. Kamaya, K. Homma, Y. Yamakawa, M. Hirayama, R. Kanno, M. Yonemura, T. Kamiyama, Y. Kato, S. Hama, K. Kawamoto, A. Mitsui, *Nat. Mater.* **2011**, *10*, 682.
[9] T. Krauskopf, F. H. Richter, W. G. Zeier, J. Janek, *Chem. Rev.* **2020**, *120*, 7745.
[10] M. Bertrand, S. Rousselot, D. Aymé-Perrot, M. Dollé, *Mater. Adv.* **2021**, *2*, 2989.
[11] J.-H. Seo, H. Nakaya, Y. Takeuchi, Z. Fan, H. Hikosaka, R. Rajagopalan, E. D. Gomez, M. Iwasaki, C. A. Randall, *J. Eur. Ceram. Soc.* **2020**, *40*, 6241.
[12] A. Kim, S. Woo, M. Kang, H. Park, B. Kang, *Front. Chem.* **2020**, *8*, 468.
[13] S. V. Patel, S. Banerjee, H. Liu, P. Wang, P.-H. Chien, X. Feng, J. Liu, S. P. Ong, Y.-Y. Hu, *Chem. Mater.* **2021**, *33*, 1435.
[14] M. Shoji, E. Jianfeng Cheng, T. Kimura, K. Kanamura, *J. Phys. D: Appl. Phys.* **2019**, *52*, 103001.
[15] W. Zhang, D. A. Weber, H. Weigand, T. Arlt, I. Manke, D. Schröder, R. Koerver, T. Leichtweiss, P. Hartmann, W. G. Zeier, J. Janek, *ACS Appl. Mater. Interfaces* **2017**, *9*, 17835.
[16] R. Koerver, I. Aygün, T. Leichtweiß, C. Dietrich, W. Zhang, J. O. Binder, P. Hartmann, W. G. Zeier, J. Janek, *Chem. Mater.* **2017**, *29*, 5574.
[17] P. Zou, Z. Lin, M. Fan, F. Wang, Y. Liu, X. Xiong, *Appl. Surf. Sci.* **2020**, *504*, 144506.
[18] X. Li, W. Peng, R. Tian, D. Song, Z. Wang, H. Zhang, L. Zhu, L. Zhang, *Electrochim. Acta* **2020**, *363*, 137185.
[19] D. H. S. Tan, E. A. Wu, H. Nguyen, Z. Chen, M. A. T. Marple, J.-M. Doux, X. Wang, H. Yang, A. Banerjee, Y. S. Meng, *ACS Energy Lett.* **2019**, *4*, 2418.
[20] S. Wang, R. Fang, Y. Li, Y. Liu, C. Xin, F. H. Richter, C.-W. Nan, *J. Materiomics* **2021**, *7*, 209.
[21] F. Walther, R. Koerver, T. Fuchs, S. Ohno, J. Sann, M. Rohnke, W. G. Zeier, J. Janek, *Chem. Mater.* **2019**, *31*, 3745.
[22] A. Banerjee, X. Wang, C. Fang, E. A. Wu, Y. S. Meng, *Chem. Rev.* **2020**, *120*, 6878.
[23] J. Zhang, H. Zhong, C. Zheng, Y. Xia, C. Liang, H. Huang, Y. Gan, X. Tao, W. Zhang, *J. Power Sources* **2018**, *391*, 73.
[24] K. Takada, N. Ohta, L. Zhang, K. Fukuda, I. Sakaguchi, R. Ma, M. Osada, T. Sasaki, *Solid State Ionics* **2008**, *179*, 1333.
[25] S. Yubuchi, S. Teragawa, K. Aso, K. Tadanaga, A. Hayashi, M. Tatsumisago, *J. Power Sources* **2015**, *293*, 941.
[26] S. Ito, S. Fujiki, T. Yamada, Y. Aihara, Y. Park, T. Y. Kim, S.-W. Baek, J.-M. Lee, S. Doo, N. Machida, *J. Power Sources* **2014**, *248*, 943.
[27] D. Kitsche, Y. Tang, Y. Ma, D. Goonetilleke, J. Sann, F. Walther, M. Bianchini, J. Janek, T. Brezesinski, *ACS Appl. Energy Mater.* **2021**, *4*, 7338.
[28] Y.-Q. Zhang, Y. Tian, Y. Xiao, L. J. Miara, Y. Aihara, T. Tsujimura, T. Shi, M. C. Scott, G. Ceder, *Adv. Energy Mater.* **2020**, *10*, 1903778.
[29] J. Cho, Y. Jeong Kim, B. Park, *Chem. Mater.* **2000**, *12*, 3788.
[30] J.-Y. Liao, A. Manthiram, *J. Power Sources* **2015**, *282*, 429.
[31] R. S. Negi, S. P. Culver, A. Mazilkin, T. Brezesinski, M. T. Elm, *ACS Appl. Mater. Interfaces* **2020**, *12*, 31392.
[32] R. S. Negi, S. P. Culver, M. Wiche, S. Ahmed, K. Volz, M. T. Elm, *Phys. Chem. Chem. Phys.* **2021**, *23*, 6725.
[33] L. Liu, *Solid State Ionics* **2002**, *152–153*, 341.
[34] M. J. Herzog, N. Gauquelin, D. Esken, J. Verbeeck, J. Janek, *Energy Technol.* **2021**, *9*, 2100028.
[35] W. Zhu, X. Huang, T. Liu, Z. Xie, Y. Wang, K. Tian, L. Bu, H. Wang, L. Gao, J. Zhao, *Coatings* **2019**, *9*, 92.
[36] X. Wen, K. Liang, L. Tian, K. Shi, J. Zheng, *Electrochim. Acta* **2018**, *260*, 549.
[37] X. Li, J. Liu, M. Norouzi Banis, A. Lushington, R. Li, M. Cai, X. Sun, *Energy Environ. Sci.* **2014**, *7*, 768.
[38] A. Garcia, *Solid State Ionics* **1990**, *40*, 13.
[39] R. S. Negi, E. Celik, R. Pan, R. Stäglich, J. Senker, M. T. Elm, *ACS Appl. Energy Mater.* **2021**, *4*, 3369.
[40] B. Han, T. Paulauskas, B. Key, C. Peebles, J. S. Park, R. F. Klie, J. T. Vaughey, F. Dogan, *ACS Appl. Mater. Interfaces* **2017**, *9*, 14769.
[41] G. Oh, M. Hirayama, O. Kwon, K. Suzuki, R. Kanno, *Chem. Mater.* **2016**, *28*, 2634.
[42] J. Ha Woo, J. E. Trevey, A. S. Cavanagh, Y. Seok Choi, S. Cham Kim, S. M. George, K. Hwan Oh, S.-H. Lee, *J. Electrochem. Soc.* **2012**, *159*, A1120.
[43] K. Takada, N. Ohta, L. Zhang, X. Xu, B. Thi Hang, T. Ohnishi, M. Osada, T. Sasaki, *Solid State Ionics* **2012**, *225*, 594.
[44] S. P. Culver, R. Koerver, W. G. Zeier, J. Janek, *Adv. Energy Mater.* **2019**, *9*, 1900626.
[45] W. B. Hawley, J. Li, *J. Energy Storage* **2019**, *25*, 100862.
[46] R. L. Puurunen, *J. Appl. Phys.* **2005**, *97*, 121301.
[47] C. Geng, S. Trussler, M. B. Johnson, N. Zaker, B. Scott, G. Botton, J. R. Dahn, *J. Electrochem. Soc.* **2020**, *167*, 110509.
[48] Y. Moryson, F. Walther, J. Sann, B. Mogwitz, S. Ahmed, S. Burkhardt, L. Chen, P. J. Klar, K. Volz, S. Fearn, M. Rohnke, J. Janek, *ACS Appl. Energy Mater.* **2021**, *4*, 7168.
[49] B. Han, B. Key, S. H. Lapidus, J. C. Garcia, H. Iddir, J. T. Vaughey, F. Dogan, *ACS Appl. Mater. Interfaces* **2017**, *9*, 41291.
[50] T. Teranishi, Y. Yoshikawa, M. Yoneda, A. Kishimoto, J. Halpin, S. O'Brien, M. Modreanu, I. M. Povey, *ACS Appl. Energy Mater.* **2018**, *1*, 3277.
[51] S.-K. Otto, Y. Moryson, T. Krauskopf, K. Peppler, J. Sann, J. Janek, A. Henss, *Chem. Mater.* **2021**, *33*, 859.
[52] F. He, d. Fang, J. Xie, L. Xue, *J. Wuhan Univ. Technol. Mater. Sci. Ed.* **2020**, *35*, 711.
[53] H. Hemmelmann, J. K. Dinter, M. T. Elm, *Adv. Mater. Interfaces* **2021**, *8*, 2002074.
[54] W. Tang, Z. Chen, F. Xiong, F. Chen, C. Huang, Q. Gao, T. Wang, Z. Yang, W. Zhang, *J. Power Sources* **2019**, *412*, 246.
[55] Y. Zhu, X. He, Y. Mo, *ACS Appl. Mater. Interfaces* **2015**, *7*, 23685.
[56] A. Jena, Y. Meesala, S.-F. Hu, H. Chang, R.-S. Liu, *ACS Energy Lett.* **2018**, *3*, 2775.
[57] R. S. Negi, P. Minnmann, R. Pan, S. Ahmed, M. Herzog, K. Volz, R. Takata, F. Schmidt, J. Janek, M. T. Elm, *Chem. Mater.* **2021**, *33*, 6713.
[58] R. Pan, D. Rau, Y. Moryson, J. Sann, J. Janek, *ACS Appl. Energy Mater.* **2020**, *3*, 6065.
[59] J. Moškon, M. Gaberščck, *J. Power Sources Advances* **2021**, *7*, 100047.
[60] N. Ogihara, S. Kawauchi, C. Okuda, Y. Itou, Y. Takeuchi, Y. Ukyo, *J. Electrochem. Soc.* **2012**, *159*, A1034.
[61] J. Bisquert, *Phys. Chem. Chem. Phys.* **2000**, *2*, 4185.